Fully Magnetically Polarized Ultrathin La$_{0.8}$Sr$_{0.2}$MnO$_3$ Films

Federico Stramaglia, Gyanendra Panchal, Frithjof Nolting, and Carlos A. F. Vaz*

Read Online

ACCESS | Metrics & More | Article Recommendations

ABSTRACT: We report the observation of fully magnetically polarized ultrathin La$_{0.8}$Sr$_{0.2}$MnO$_3$ films by using LaMnO$_3$ and La$_{0.45}$Sr$_{0.55}$MnO$_3$ buffer layers grown epitaxially on SrTiO$_3$(001) substrates by molecular beam epitaxy. Specifically, we show that La$_{0.8}$Sr$_{0.2}$MnO$_3$ films grown on 12-unit-cell LaMnO$_3$ have bulk-like magnetic moments starting from a single unit cell thickness, while for the 15-unit-cell La$_{0.45}$Sr$_{0.55}$MnO$_3$ buffer layer, the La$_{0.8}$Sr$_{0.2}$MnO$_3$ transitions from an antiferromagnetic state to a fully spin-polarized ferromagnetic state at 4 unit cells. The magnetic results are confirmed by X-ray magnetic circular dichroism, while linear dichroic measurements carried out for the La$_{0.8}$Sr$_{0.2}$MnO$_3$/La$_{0.45}$Sr$_{0.55}$MnO$_3$ series show the presence of an orbital reorganization at the transition from the antiferromagnetic to ferromagnetic state corresponding to a change from a preferred in-plane orbital hole occupancy, characteristic of the A-type antiferromagnetic state of La$_{0.45}$Sr$_{0.55}$MnO$_3$, to preferentially out of plane. We interpret our findings in terms of the different electronic charge transfers between the adjacent layers, confined to the unit cell in the case of insulating LaMnO$_3$ and extended to a few unit cells in the case of conducting La$_{0.45}$Sr$_{0.55}$MnO$_3$. Our work demonstrates an approach to growing ultrathin mixed-valence manganite films that are fully magnetically polarized from the single unit cell, paving the way to fully exploring the unique electronic properties of this class of strongly correlated oxide materials.

KEYWORDS: *mixed-valence manganites, ultrathin films, oxide heterostructures, antiferromagnetic spintronics, molecular beam epitaxy, complex oxides*
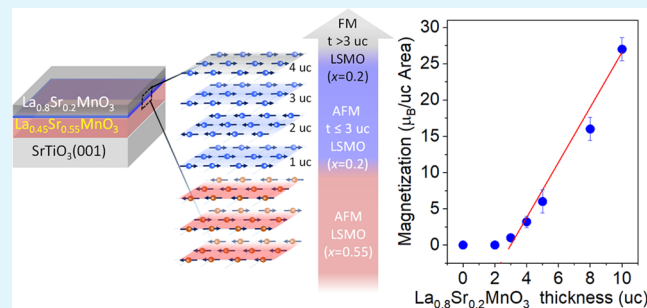
1. INTRODUCTION

The disruption of the atomic structure at the boundary between different materials often gives rise to the emergence of new phenomena that are characteristic of the interface region itself.[1,2] The study of such interface phenomena is important to understanding the role of broken symmetries, electron exchange, and correlation effects to the electronic properties, but may also hold promise for new electronic devices based on purely interfacial effects. Critical for strong interfacial effects is the growth of sharp and well-defined interfaces separating materials with pristine electronic structures; this is because the presence of defects at the interface may strongly disturb the electronic properties of the component phases, for instance, making the interdiffused interface of a magnetic material nonmagnetic[3] or where the presence of charge traps screens the polarization of a ferroelectric interface.[4]

One example of an interfacial effect is the onset of a magnetoelectric coupling emerging at the boundary between ferromagnetic and ferroelectric materials to form multiferroic heterostructures, whereby control of magnetism through electric fields is made possible.[4−10] For the particular case of the Pb(Zr$_{0.2}$Ti$_{0.8}$)O$_3$/La$_{0.8}$Sr$_{0.2}$MnO$_3$ interface, the magnetoelectric coupling was demonstrated to originate from charge-driven modulation of the valency and spin configuration of the

interfacial La$_{0.8}$Sr$_{0.2}$MnO$_3$ layer induced by charge screening of the ferroelectric polarization.[11] The large magnetoelectric coupling engineered in this system exploited the rich functional properties and complex phase diagrams of the mixed-valence manganites characterized by multiple electronic ground states.[12−16] The observed changes in the magnetic moment of the La$_{0.8}$Sr$_{0.2}$MnO$_3$ layer are on the order of 20%, which is a large effect; however, given the interfacial character of the magnetoelectric coupling, the change in the magnetic moment is associated with only a few unit cells of the whole sample, and therefore, the total change is averaged out by the remainder of the magnetic film. The latter has a lower thickness limit determined by the magnetic and electric behaviors of La$_{1−x}$Sr$_x$MnO$_3$ thin films: when grown on high-quality SrTiO$_3$(001) substrates, the onset of electric conductivity occurs at about 10 unit cells (uc), while the magnetic moment is strongly reduced and is absent below 5 uc,[17,18] forming
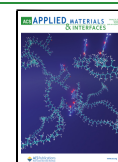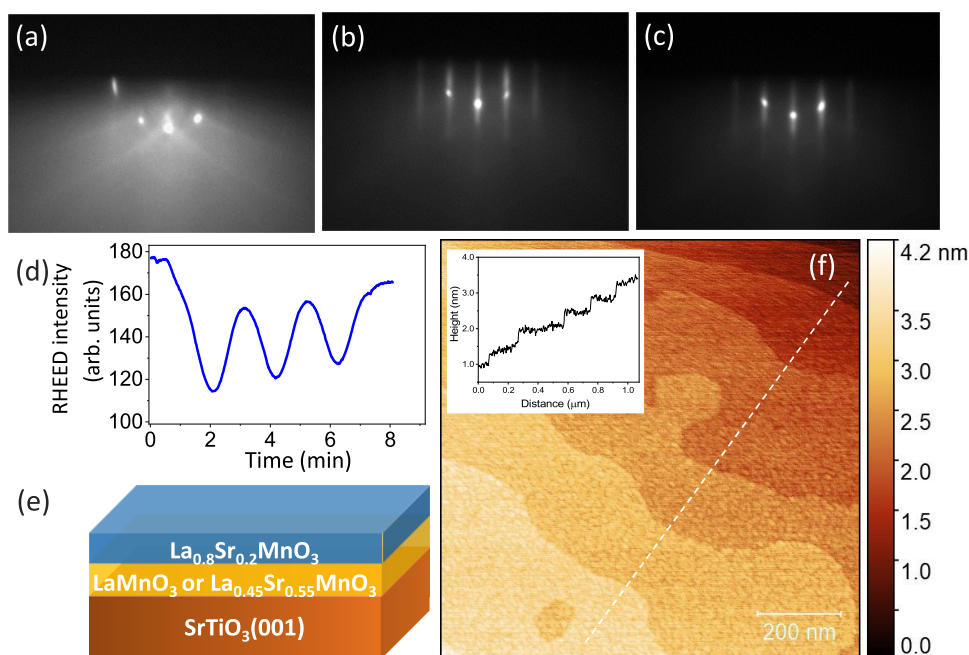
Figure 1. (a–c) RHEED patterns of the TiO_2-terminated $SrTiO_3(001)$ substrate, the $LaMnO_3$ buffer layer, and the 3 uc $La_{0.8}Sr_{0.2}MnO_3/LaMnO_3$ film, respectively, along the $\langle 100 \rangle$ azimuth. The energy of the incident electron beam was set to 15 keV. (d) RHEED intensity oscillations as a function of time for 3 uc $La_{0.8}Sr_{0.2}MnO_3$ deposited on $LaMnO_3$. (e) Schematic of the sample structure. (f) AFM measurement of the 10 uc of $La_{0.8}Sr_{0.2}MnO_3/LaMnO_3$ sample, showing a flat surface with single unit cell step terraces (inset).

magnetic and electric "dead layers", whose origin has been variously attributed to magnetic or orbital interfacial reconfiguration, cation intermixing, or polar discontinuity.[19−29] It is therefore important to devise solutions for obtaining ultrathin films with bulk-like or enhanced interfacial characteristics, including full magnetic and ferroelectric polarizations in ferromagnetic and ferroelectric systems, respectively. In addition, one also expects that the relative importance of the interfacial effect will increase as the thickness is reduced since the interface will then be a larger portion of the overall system. Hence, it is important that not only the interface is well-defined but also that the electronic properties of the materials remain robust with decreasing thickness, ideally down to the monolayer range.[3,4]

To overcome the degradation in the magnetic properties of ultrathin manganites, one strategy consists of decoupling the films from the nonmagnetic substrate by inserting a magnetically polarized buffer layer.[20,30] For example, the introduction of 2 uc $LaMnO_3$ between a 120 nm thick $La_{1−x}Sr_xMnO_3$ ($x = 0.4$) and the $SrTiO_3$ substrate leads to the disappearance of the dead layer as measured by second harmonic signal generation and ascribed to the interruption of charge transfer across the $SrTiO_3$ interface, which is otherwise responsible for hole doping of the $La_{0.6}Sr_{0.4}MnO_3$ film.[20] In another instance, 1 uc $La_{1−x}Ba_xMnO_3(x = 0.3)$ films sandwiched between two 3 uc $SrRuO_3$ layers are found to be fully magnetically polarized, an effect attributed to the presence of oxygen octahedral rotations induced by $SrRuO_3$, leading to an orbital reconstruction and an enhancement of the interfacial magnetic properties.[31] In another example, $CaRu_{1/2}Ti_{1/2}O_3$ used as an interlayer in $La_{2/3}Ca_{1/3}MnO_3$ superlattices has been shown to preserve the magnetic properties of the individual manganite films and to result in antiferromagnetic interlayer coupling.[32] These studies highlight the importance of separating the manganite film from the supporting $SrTiO_3$ substrate and highlight the role of charge

transfer, spin exchange, and octahedral tilting, together with orbital rearrangement, in the improvement of the magnetic properties toward bulk characteristics.

In this study, we explore the magnetic and transport properties of ultrathin $La_{0.8}Sr_{0.2}MnO_3$ films when a manganite buffer layer is introduced at the interface with the $SrTiO_3$ substrate. We employ two different types of buffer layers, a nominally antiferromagnetic insulating $LaMnO_3$ and an antiferromagnetic conducting $La_{0.45}Sr_{0.55}MnO_3$, in order to disentangle the roles of spin and charge exchange at the interface. In the first case, our results show that the $La_{0.8}Sr_{0.2}MnO_3$ film develops robust magnetic properties, with a near-bulk-like critical temperature and magnetic moments that are independent of thickness starting at 1 uc. In the second case, an antiferromagnetic coupling to the buffer layer is observed for thicknesses up to 3 uc, while for larger thicknesses, the top $La_{0.8}Sr_{0.2}MnO_3$ layer transitions to a fully polarized ferromagnetic state. By probing the electronic band structure using X-ray absorption spectroscopy, we link the magnetic properties of $La_{0.8}Sr_{0.2}MnO_3$ to the evolution of orbital occupancy with film thickness.

2. EXPERIMENTAL SECTION

The samples in this study consist of $La_{0.8}Sr_{0.2}MnO_3$ films with thicknesses ranging from 0 to 10 uc, grown on a 12 uc $LaMnO_3$ buffer layer (except for the 3 uc $La_{0.8}Sr_{0.2}MnO_3$ sample, grown on 14 uc $LaMnO_3$) or on a 15 uc $La_{0.45}Sr_{0.55}MnO_3$ buffer layer. Figure 1e shows a schematic diagram of the sample structure. The buffer layer thickness is chosen based on previous works showing that 12 uc $LaMnO_3$ is insulating and has a reduced magnetic moment[33] and that 15 uc $La_{0.45}Sr_{0.55}MnO_3$ is conducting antiferromagnetic.[34] The samples were grown in an oxide molecular beam epitaxy (MBE) system with a base pressure of $2 \times 10^{−10}$ mbar, equipped with five effusion cells, a reflection high-energy electron diffraction (RHEED) system, and a load-lock chamber for sample transfer. For this study, we used commercially available $SrTiO_3(001)$ substrates (SurfaceNet), with $\pm 0.1°$ miscut,

which were chemically treated with a HCl:HNO$_3$ solution and annealed to 1000 °C in air to provide single TiO$_2$-terminated surfaces.[35,36] For metal oxide deposition, we set the molecular oxygen partial pressure to $(5 \pm 1) \times 10^{-7}$ mbar, the substrate temperature to 720 °C, and the evaporation rate to about 0.5 uc/min, values that we found to provide the optimal growth conditions. In all cases, we adopted the same procedure for preparing the SrTiO$_3$ substrate *in situ*, which consisted of heating slowly the substrate up to the growth temperature so as to keep the pressure below 2×10^{-7} mbar and below 2×10^{-9} mbar before growth. The surface of the SrTiO$_3$(001) substrate was always monitored before and during the film growth and showed a similar RHEED pattern across the sample series. The evaporation rates are determined for each material from a calibrated thickness monitor (2% error), while the La$_{0.8}$Sr$_{0.2}$MnO$_3$ thickness was monitored in real time by following the RHEED intensity oscillations; for the buffer layer, it was not possible to determine the exact thickness exclusively on the basis of the RHEED oscillations since they are not observable at the early stages of deposition. The LaMnO$_3$ and La$_{0.45}$Sr$_{0.55}$MnO$_3$ thicknesses are hence estimated from the total growth time and the deposition rate, estimated by the RHEED oscillations appearing later in the deposition process. For this reason, we take into account an experimental error of 1 uc in the LaMnO$_3$ thickness. In Figure 1a–c, we show representative RHEED patterns for the TiO$_2$-terminated SrTiO$_3$ substrate, LaMnO$_3$, and La$_{0.8}$Sr$_{0.2}$MnO$_3$ films after growth, respectively, demonstrating epitaxial growth and good surface properties. The observation of RHEED intensity oscillations, as illustrated in Figure 1d for the 3 uc La$_{0.8}$Sr$_{0.2}$MnO$_3$/LaMnO$_3$ film, indicates layer-by-layer growth; from atomic force microscopy (AFM) measurements, such as shown in Figure 1f, one observes the atomic steps from the substrate with a step height of ~4 Å, i.e., of a single atomic unit cell, showing that the manganite films grow in single unit cell steps. After growth, the samples belonging to the LaMnO$_3$ series are annealed in air at 600 °C for 6 h to fully oxygenate the films. Henceforth, the samples are named with the thickness of the top La$_{0.8}$Sr$_{0.2}$MnO$_3$ layer in uc. The atomic force microscopy (AFM) measurements were performed in the tapping mode using a Bruker dimension icon 3100 instrument.

X-ray diffraction measurements were carried out in a Seifert four-circle diffractometer equipped with a Cu anode X-ray tube and a linear array detector. The measurements consisted of θ−2θ scans along the (002) diffraction peak to determine the out-of-plane lattice parameter and reciprocal space mapping scans around the (103) diffraction peak to extract the in-plane lattice parameter. The transport properties were measured in a home-built four-probe setup in a van der Pauw configuration,[37,38] which uses spring contacts for a fast measurement setup; one drawback is that it leads to strong variations in the contact resistance, which we attribute to surface adsorbates due to the high vacuum or to surface residues from previous cleaning steps, making estimates of the absolute resistivity difficult. SQUID magnetometry measurements were performed using a 7 T Quantum Design MPMS3−137 magnetic properties measurement system (MPMS) with the magnetic field applied along the film plane. X-ray absorption spectroscopy (XAS) measurements were carried out at the SIM and X-Treme beamlines at the Swiss Light Source (SLS) at the Paul Scherrer Institute (PSI), Switzerland, with the signal collected in the total electron yield (TEY) mode, which has a high surface sensitivity due to the limited mean free path of the electrons in solid materials on the order of 3 nm, or about 8 uc, and the exponential attenuation of the TEY signal with thickness. When measuring at SIM, before each magnetic XAS measurement, a saturation field of 1 kOe was applied to the sample and the measurements were performed under a 200 Oe magnetic field. At X-Treme, the saturation field was 6 T and the measurements were performed at remanence. We collected XAS spectra with circularly left and right polarized light, from which we obtained the unpolarized (average) spectra and the X-ray magnetic circular dichroism (XMCD) spectra (difference). The latter are normalized by dividing it by the L$_3$ peak intensity of the respective average XAS spectrum to give the dichroic signal as a percentage of the average XAS spectrum. Linear dichroism measurements were carried out by measuring the XAS spectra with the sample at a normal angle of incidence and at 45° to the X-ray beam to probe, respectively, the in-

plane and out-of-plane orbital states; for one sample (5 uc La$_{0.8}$Sr$_{0.2}$MnO$_3$/La$_{0.45}$Sr$_{0.55}$MnO$_3$), the X-ray linear dichroic (XLD) measurements were carried out using the X-ray photoemission electron microscope at the SIM beamline, where the light impinges the sample at a grazing angle of 16°. The different experimental conditions for these measurements (i.e., different monochromator grating and beam slit settings) result in a lower energy resolution of the 5 uc spectra. In order to compare spectra taken at different geometries, the out-of-plane XAS spectra are calculated using the expression for the angular dependence of the linear dichroism, $I(\theta) = I_{ab} \cos^2 \theta + I_c \sin^2 \theta$, where θ is the angle of incidence of the light with respect to the sample surface and I_{ab} and I_c are the X-ray absorption parallel to the sample surface and perpendicular to it, respectively.

3. RESULTS AND DISCUSSION

To determine the strain state of the heterostructures, we carried out X-ray diffraction measurements on the two 10 uc La$_{0.8}$Sr$_{0.2}$MnO$_3$ films. The θ−2θ scans around the (002) SrTiO$_3$ peak are shown in Figure 2a,b for the LaMnO$_3$ and
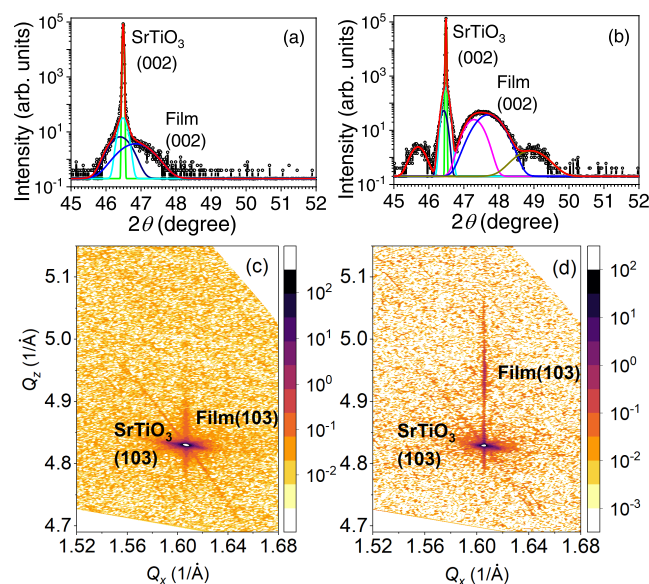
Figure 2. θ−2θ X-ray diffraction scans for (a) 10 uc La$_{0.8}$Sr$_{0.2}$MnO$_3$/LaMnO$_3$ and (b) 10 uc La$_{0.8}$Sr$_{0.2}$MnO$_3$/La$_{0.45}$Sr$_{0.55}$MnO$_3$ heterostructures. Reciprocal space mapping around the asymmetric (103) Bragg reflection of SrTiO$_3$ for (c) 10 uc La$_{0.8}$Sr$_{0.2}$MnO$_3$/LaMnO$_3$ and (d) 10 uc La$_{0.8}$Sr$_{0.2}$MnO$_3$/La$_{0.45}$Sr$_{0.55}$MnO$_3$. The vertical scale represents the scattering intensity in arbitrary units.

La$_{0.45}$Sr$_{0.55}$MnO$_3$ buffer layers, respectively. In both cases, broad peaks to the right of the (002) SrTiO$_3$ line are observed, corresponding to the pseudocubic (002) planes of the manganite films; in the case of the LaMnO$_3$ buffer layer, only one peak can be distinguished. By fitting the peak with three Gaussian components (Figure 2a), one for the SrTiO$_3$ peak together with a diffused scattering component and a third for the LaMnO$_3$/La$_{0.8}$Sr$_{0.2}$MnO$_3$ bilayer, we obtain for the latter an out-of-plane lattice parameter of 3.87 Å, which is below both LaMnO$_3$ and La$_{0.8}$Sr$_{0.2}$MnO$_3$ pseudocubic bulk values of $a/\sqrt{2}$ = 3.89 Å.[13] For the case of the film with the La$_{0.45}$Sr$_{0.55}$MnO$_3$ buffer layer, we observe the presence of clear Laue oscillations, indicative of high-quality interfaces and that the manganite peak is composed of two overlapping components (Figure 2b), which we ascribe to the La$_{0.8}$Sr$_{0.2}$MnO$_3$ and La$_{0.45}$Sr$_{0.55}$MnO$_3$ films. By fitting this peak to two Gaussian components together with the SrTiO$_3$ peak with a diffused scattering component, we obtain
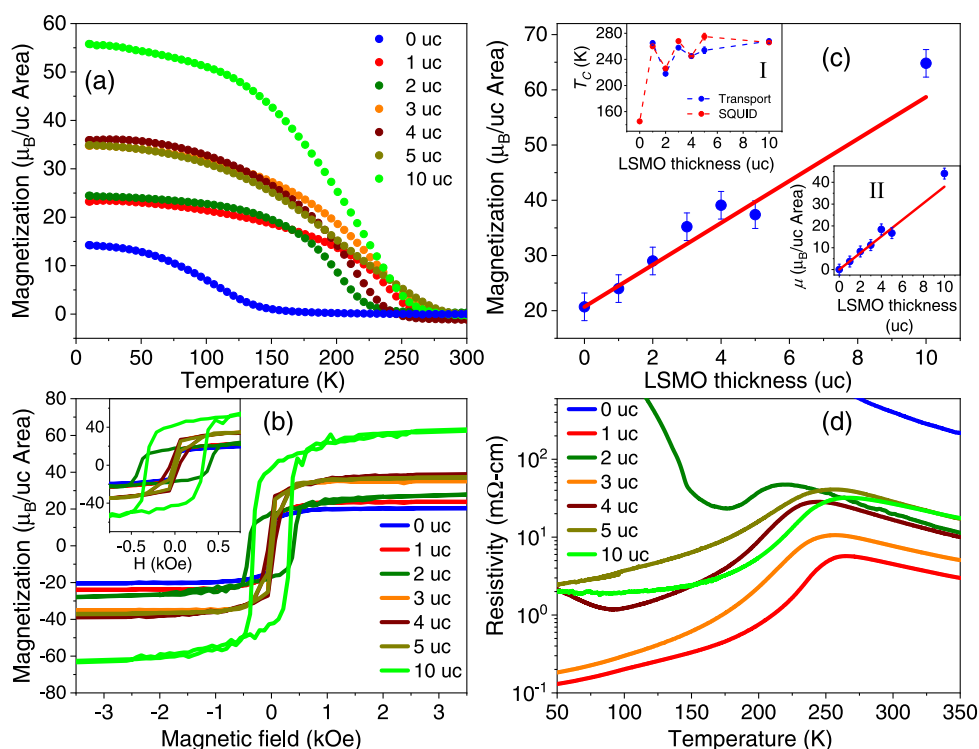
Figure 3. (a) Field-cooled magnetization variation with temperature of the $La_{0.8}Sr_{0.2}MnO_3/LaMnO_3$ films taken during heating (applied magnetic field of 1 kOe). (b) Magnetic hysteresis curves at 20 K. Inset: Zoomed-in $M{-}H$ curves highlighting the low field magnetic behavior. (c) Zero-field saturation magnetization per unit cell area versus $La_{0.8}Sr_{0.2}MnO_3$ film thickness (symbols) extrapolated from the $M{-}H$ loops; the red line has a slope of 3.8 μ_B/uc. Inset (I) shows the variation of the critical temperature (SQUID) and of the peak in resistivity as a function of $La_{0.8}Sr_{0.2}MnO_3$ film thickness (dashed lines are guides to the eye); inset (II) shows the magnetic moment (μ) variation without the $LaMnO_3$ moment contribution. The error bars in the magnetization are related to the experimental uncertainty due to the $LaMnO_3$ thickness. (d) Resistivity versus temperature for the $La_{0.8}Sr_{0.2}MnO_3/LaMnO_3$ sample series.

out-of-plane lattice parameters of 3.84 and 3.81 Å, which we assign to the $La_{0.8}Sr_{0.2}MnO_3$ and $La_{0.45}Sr_{0.55}MnO_3$ films, respectively. These values are considerably smaller than the respective pseudocubic bulk lattice parameters of 3.89 and 3.84 Å,[13,34,39] as expected for the tensile strain induced by the $SrTiO_3$ substrate.

Reciprocal space mapping (RSM) around the asymmetric (103) plane of $SrTiO_3$ is shown in Figure 2c,d for $La_{0.8}Sr_{0.2}MnO_3/LaMnO_3$ and $La_{0.8}Sr_{0.2}MnO_3/La_{0.45}Sr_{0.55}MnO_3$, respectively. One finds that the Bragg reflection corresponding to the film bilayer lies at the same Q_x value for both heterostructures, which directly shows that the manganite films grow coherently to the $SrTiO_3$ substrate and are fully strained. We expect likewise the thinner $La_{0.8}Sr_{0.2}MnO_3$ films to be also fully strained to the $SrTiO_3$ substrate.

The temperature dependence of the magnetization ($M{-}T$) of the ultrathin $La_{0.8}Sr_{0.2}MnO_3/LaMnO_3$ films as a function of $La_{0.8}Sr_{0.2}MnO_3$ thickness is shown in Figure 3a. A first observation is that the 12 uc $LaMnO_3/SrTiO_3$ (001) film exhibits a nonzero saturation magnetization, which is not expected for stoichiometric bulk $LaMnO_3$ but is similar to what has been reported previously in the literature for $LaMnO_3$ thin films.[40−47] The Curie temperature, T_C = 145 K, is coincidentally very close to the Néel temperature of bulk $LaMnO_3$, of 143 K.[13] While the origin of magnetism in $LaMnO_3$ is still under debate, recent surface-sensitive X-ray photoemission spectroscopy measurements indicate the presence of Sr and Ca in the $LaMnO_3$ film in both the as-grown and annealed states of up to a few %, suggesting that the magnetic moment in $LaMnO_3$ may be

driven in large part by doping from divalent cations diffusing from the substrate.[48] For the $La_{0.8}Sr_{0.2}MnO_3$ films, the results show that starting from 1 uc $La_{0.8}Sr_{0.2}MnO_3$, the Curie temperature jumps to T_C = 260 K (compared with 309 K for bulk $La_{0.8}Sr_{0.2}MnO_3$ and 305 K for thick $La_{0.8}Sr_{0.2}MnO_3/$STO(001), slightly reduced from the bulk value due to epitaxial tensile strain);[13,17] with increasing $La_{0.8}Sr_{0.2}MnO_3$ thickness, T_C is seen to oscillate around 250 K, as shown in inset I of Figure 3c, which could be a manifestation of finite-size effects.[3] Notably, we find no independent contribution from the $LaMnO_3$ buffer layer in the $M{-}T$ curves, indicating that the two layers are fully coupled magnetically. We also observe a steady increase in the saturation magnetization with increasing thickness, which we quantify from magnetic hysteresis curves carried out at 20 K, shown in Figure 3b. These data show that the $La_{0.8}Sr_{0.2}MnO_3$ films have small coercive fields, of ∼50 Oe, except for the 2 and 10 uc $La_{0.8}Sr_{0.2}MnO_3$ films, which exhibit coercive fields of ∼300 Oe. We attribute the larger coercive field to sample-to-sample growth-related variations. The larger coercivity implies stronger energy barriers to domain wall motion or to nucleation of reverse domains; given the high sensitivity of the coercive field to extrinsic factors, including local structural variations induced by the substrate morphology (such as degree of miscut, surface roughness, and point defects), some variation in the coercive field may be expected. By extrapolating from the high field region to zero field, we estimate the zero-field saturation magnetization as a function of thickness, shown in Figure 3c, to find that the saturation moment increases linearly with thickness, with a slope of 3.8 μ_B/uc expected for bulk
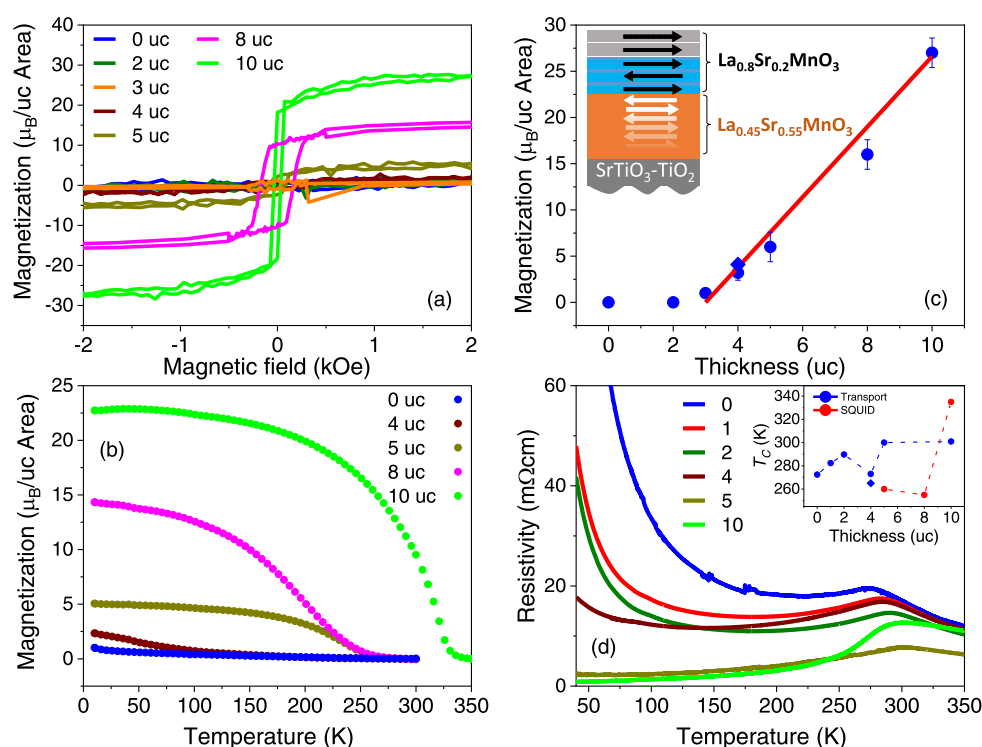
Figure 4. (a) Magnetization hysteresis curves of the $La_{0.8}Sr_{0.2}MnO_3/La_{0.45}Sr_{0.55}MnO_3$ sample series (20 K) and (b) magnetization temperature dependence of the 0, 4, 5, 8, and 10 uc $La_{0.8}Sr_{0.2}MnO_3$ films (1 kOe). (c) Zero-field saturation moments extrapolated from the $M-H$ loops. The red line has a slope of 3.8 μ_B/uc crossing the abscissa at 3 uc. Inset: Schematic representation of the magnetic spin configuration of the $La_{0.8}Sr_{0.2}MnO_3$ film on the $La_{0.45}Sr_{0.55}MnO_3$ buffer layer. (d) Transport measurements showing the evolution of the temperature-dependent resistivity with thickness. The metal-to-insulator transition variation with thickness, identified as T_C, is shown in the figure inset together with the Curie temperature, obtained as a linear extrapolation to zero from the $M-T$ curves. The diamond symbols in (c) and (d) are from a second 4 uc $La_{0.8}Sr_{0.2}MnO_3/La_{0.45}Sr_{0.55}MnO_3$ sample grown subsequently.

$La_{0.8}Sr_{0.2}MnO_3$, shown as a red line. This result demonstrates that the insertion of a $LaMnO_3$ buffer layer results in $La_{0.8}Sr_{0.2}MnO_3$ films that are fully magnetically polarized down to 1 uc. The intercept at the origin gives the magnetization of $LaMnO_3$, of 20.7 μ_B/uc area, corresponding to an average magnetic moment of 1.7 μ_B/Mn, in agreement with previous findings in the literature.[42,47] Assuming the $LaMnO_3$ moment to be constant throughout the sample series, we can subtract its (constant) magnetic contribution to obtain the linear behavior shown in inset II of Figure 3c. For the 3 uc $La_{0.8}Sr_{0.2}MnO_3$ thickness, we expect a slightly larger magnetic moment due to the thicker $LaMnO_3$ layer (14 uc), and in inset II of Figure 3c, we show the magnetic moment after subtracting an additional moment of 3.4 μ_B corresponding to the extra 2 uc $LaMnO_3$. These results highlight the fact that the $La_{0.8}Sr_{0.2}MnO_3$ films develop a full magnetic moment starting from the first unit cell. In our discussion, we have supposed that no interdiffusion between the two layers occurs, i.e., that the two layers are well-defined. This is supported by our results: a systematic increase in the saturation magnetization as a function of the top $La_{0.8}Sr_{0.2}MnO_3$ thickness of 3.8 μ_B/uc indicates that inter-diffusion, if present, is not the major factor driving the observed phenomena.

The transport properties are listed in Figure 3d. A first remark is that the relative variation of the resistivity with $La_{0.8}Sr_{0.2}MnO_3$ film thickness does not follow the expected behavior, namely, a decrease with increasing film thickness. We attribute this largely to contact resistance introduced by the spring contacts in our measurement setup; coincidentally, the 2 and 10 uc $La_{0.8}Sr_{0.2}MnO_3$ films showing a larger coercive field also have

a systematically larger resistivity, a property which is also very sensitive to local morphological and structural variations. However, while the presence of defects in the samples is expected to impact the resistivity and coercive field, we find that it does not strongly affect the saturation moments, as the $M-H$ curves indicate. From the temperature dependence, we find that the 12 uc thick $LaMnO_3$ film is insulating, consistent with previous reports and as expected for bulk $LaMnO_3$;[13,33] importantly, starting from 1 uc thickness, the films exhibit a clear peak in the resistivity at a temperature near the magnetic critical temperature (inset I of Figure 3c), typical of the mixed-valence "colossal" magnetoresistance (CMR) manganites.[49] The 2 and 4 uc $La_{0.8}Sr_{0.2}MnO_3$ films show a second transition to insulating behavior at low temperatures, which is often found in thin $La_{0.8}Sr_{0.2}MnO_3/SrTiO_3(001)$ films and attributed to A-site disorder-induced charge localization effects.[50] These results show that also the transport properties of the ultrathin $La_{0.8}Sr_{0.2}MnO_3$ films are similar to that of the bulk counterpart.[13] The $La_{0.8}Sr_{0.2}MnO_3$ films are conducting and exhibit a metal-to-insulator transition starting from 1 uc, which demonstrates that the $La_{0.8}Sr_{0.2}MnO_3$ is in a metallic ferromagnetic state and has no electric dead layer as is the case with $La_{1-x}Sr_xMnO_3$ films grown on $SrTiO_3$, for example, and that the peak in resistivity agrees with T_c obtained from the $M-T$ curves, which is another characteristic of the mixed-valence manganites. These are important aspects for utilizing such ultrathin films for field effect devices or as polarizers in tunnel barriers.

The results for the case of $La_{0.8}Sr_{0.2}MnO_3/La_{0.45}Sr_{0.55}MnO_3$ are markedly different. The magnetic hysteresis loops, presented in Figure 4a, show that the $La_{0.45}Sr_{0.55}MnO_3/SrTiO_3(001)$ film

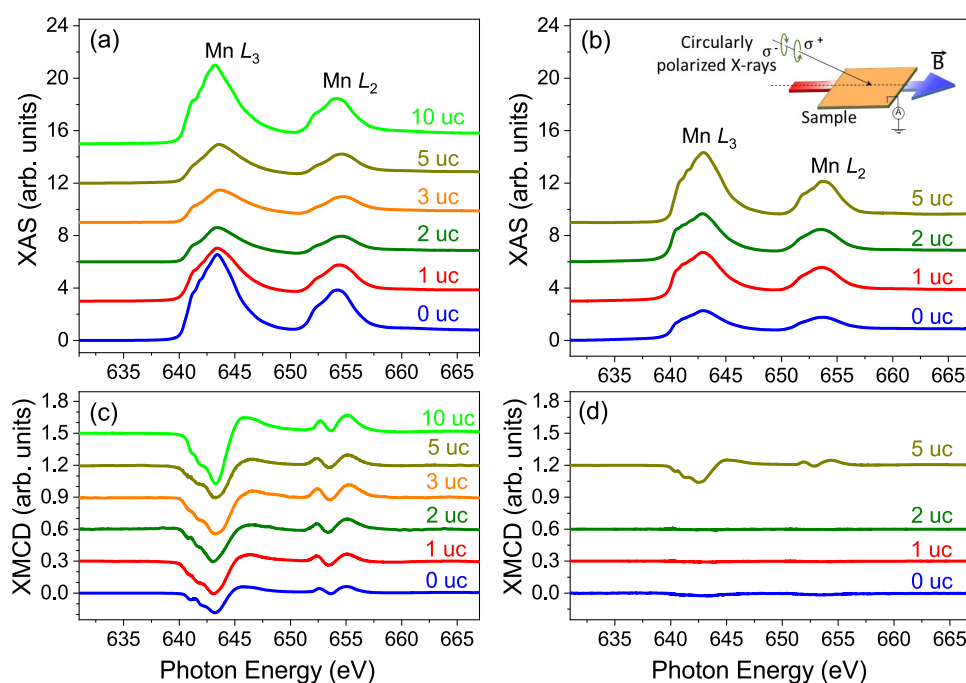**Figure 5.** XAS spectra collected on $La_{0.8}Sr_{0.2}MnO_3$ films grown on (a) the $LaMnO_3$ and (b) the $La_{0.45}Sr_{0.55}MnO_3$ buffer layer. The corresponding XMCD spectra, normalized to the respective XAS peak value, are shown in (c) and (d). All spectra are shifted vertically for clarity of display.

exhibits no magnetic hysteresis, consistent with the expected antiferromagnetic state reported earlier.[34] Also, the $La_{0.8}Sr_{0.2}MnO_3$ films up to 3 uc thickness show a negligible magnetic response to the applied magnetic field, while for thicknesses above 4 uc, magnetic hysteresis is present with coercive fields in the range from 50 to 100 Oe. The magnetic behavior is also confirmed by temperature-dependent magnetization measurements shown in Figure 4b for the 4, 5, 8, and 10 uc films, where the onset of magnetization in the system is observed at 250 K (with the 4 uc film showing an uptick in the magnetization at around 100 K; this behavior was reproduced in a second sample grown subsequently). Remarkably, the 10 uc $La_{0.8}Sr_{0.2}MnO_3$ film reaches a critical temperature of about 300 K, close to the bulk value. The saturation magnetic moment extracted from the $M-H$ curves is presented in Figure 4c and shows an approximately linear increase in magnetization for thicknesses above 3 uc with a slope of about 3.8 μ_B/uc.

The resistivity of the $La_{0.8}Sr_{0.2}MnO_3$ films grown on $La_{0.45}Sr_{0.55}MnO_3$ as a function of temperature is shown in Figure 4d. Since in this case the buffer layer brings a non-negligible contribution to the total resistivity, the latter is calculated using the bilayer film thickness. The 0 uc sample shows a metal-to-insulator transition (MIT) at T_{MIT} = 287 K, in agreement with a previous report.[34] The reduced resistivity and increased MIT temperature (T_{MIT}) of the 1, 2, and 3 uc samples show that the $La_{0.8}Sr_{0.2}MnO_3$ layers have a lower resistivity compared to the buffer layer. The 4 uc $La_{0.8}Sr_{0.2}MnO_3$/$La_{0.45}Sr_{0.55}MnO_3$ shows instead a drop in T_{MIT}, as also shown in the figure inset (we confirmed this behavior from a second 4 uc $La_{0.8}Sr_{0.2}MnO_3$/$La_{0.45}Sr_{0.55}MnO_3$ sample). A further increase in T_{MIT} is observed for the 5 and 10 uc samples, saturating at ~300 K. The critical temperature estimated from the peak resistivity is found to be significantly different from that estimated from the $M-T$ curves, a discrepancy that is much larger than that for the $La_{0.8}Sr_{0.2}MnO_3$/$LaMnO_3$ series. For example, for the 5 uc film, the critical temperature obtained from

the magnetization curve is about 260 K, while the peak in resistivity remains close to that of 3 uc $La_{0.8}Sr_{0.2}MnO_3$, of about 290 K. Differently from the previous case, where the $LaMnO_3$ buffer layer is insulating and T_{MIT} is entirely determined by the $La_{0.8}Sr_{0.2}MnO_3$ layer itself, the $La_{0.45}Sr_{0.55}MnO_3$ buffer layer is conducting; hence, the transport properties are determined by the interplay of the two layers. Therefore, although a formal distinction of the two layers cannot be done from the resistivity data, we can draw some conclusions by combining the transport and magnetization data: up to 4 uc, $La_{0.8}Sr_{0.2}MnO_3$ couples antiferromagnetically to $La_{0.45}Sr_{0.55}MnO_3$, which is inferred from the SQUID measurements and the systematic increase of T_{MIT} within this thickness range. When $La_{0.8}Sr_{0.2}MnO_3$ becomes ferromagnetic, T_{MIT} is given by a weighted average of the two contributions corresponding to the Curie (for $La_{0.8}Sr_{0.2}MnO_3$) and Néel (for $La_{0.45}Sr_{0.55}MnO_3$) temperatures. The fact that they do not agree suggests that at and above 5 uc thickness, the ferromagnetic component of the $La_{0.8}Sr_{0.2}MnO_3$ film is magnetically decoupled from the manganite layers underneath. An alternative explanation, given that one does not clearly distinguish two peaks in the resistivity, could be that the top $La_{0.8}Sr_{0.2}MnO_3$ films switch from an antiferromagnetic state at higher temperatures to the ferromagnetic ground state with decreasing temperatures. The kink at around 100 K observed for the 1–4 uc films is due to the $SrTiO_3$ cubic-to-tetragonal phase transition, which affects particularly strongly $La_{1-x}Sr_xMnO_3$ films at near the 0.5 doping.[34,51]

We interpret the results for $La_{0.8}Sr_{0.2}MnO_3$/$La_{0.45}Sr_{0.55}MnO_3$ as showing that the 1–3 uc $La_{0.8}Sr_{0.2}MnO_3$ films either are antiferromagnetic or couple antiferromagnetically to the $La_{0.45}Sr_{0.55}MnO_3$ buffer layer with the possible presence of antiferromagnetic domains in the $La_{0.45}Sr_{0.55}MnO_3$ buffer layer averaging out the net magnetization, while for larger thicknesses, the additional layer changes abruptly to a ferromagnetic state. X-ray photoemission electron microscopy results show, in fact, that for the 1–3 uc $La_{0.8}Sr_{0.2}MnO_3$ film no ferromagnetic contrast

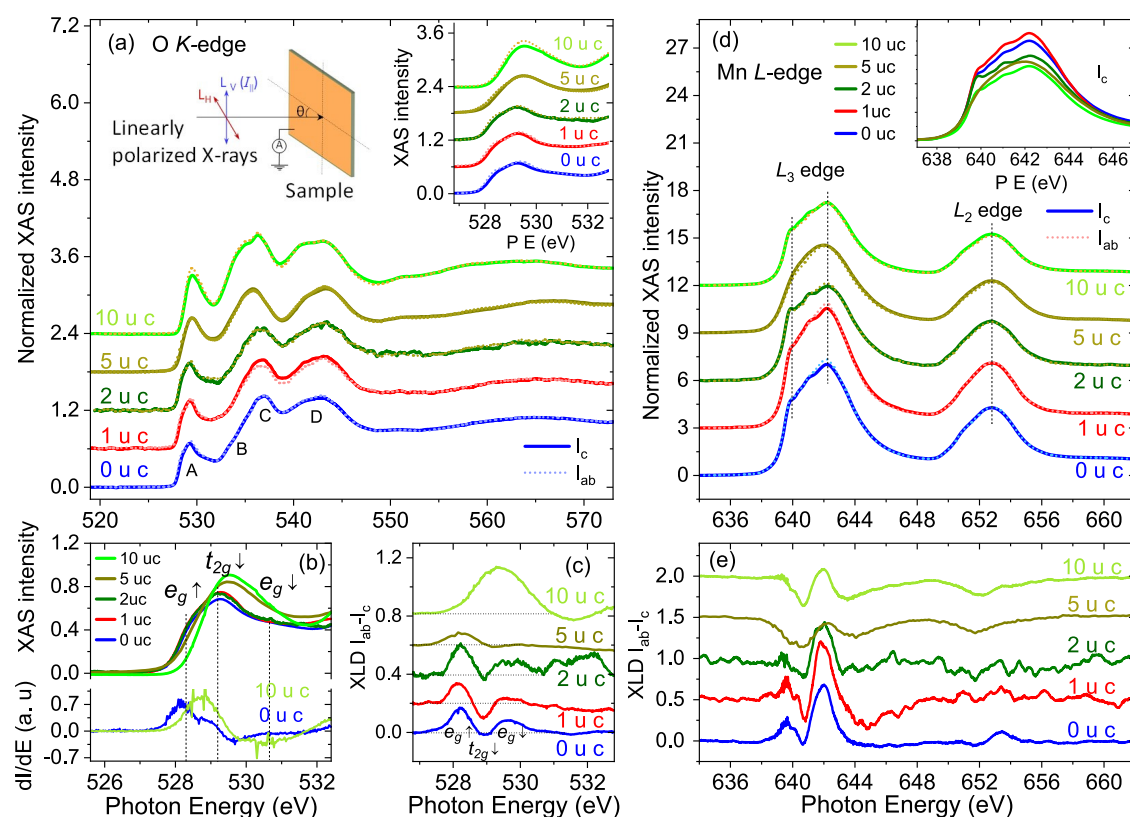**Figure 6.** (a) Room-temperature XAS spectra at the O K-edge obtained with linearly polarized light for $La_{0.8}Sr_{0.2}MnO_3/La_{0.45}Sr_{0.55}MnO_3$. (b) Detail of the pre-edge feature of the spectra (out-of-plane light polarization) highlighting the transition associated with the O 2p-Mn 3d hybridized states. The derivatives of the 1 and 10 uc spectra are also shown to highlight the peak position. (c) O K-edge XLD spectra of the $La_{0.8}Sr_{0.2}MnO_3$ films. (d) XAS spectra at the Mn L-edge collected with vertical (I_{ab}) and horizontal (I_c) light polarization. Inset shows a plot of all spectra at the L_3-edge. (e) Mn L-edge XLD spectra. Spectra are shifted vertically for clarity of display.

over an antiferromagnetic multidomain state is present, consistent with the scenario that at small thicknesses, the thinner $La_{0.8}Sr_{0.2}MnO_3$ films order antiferromagnetically.[52] The increase in the Néel temperature (corresponding to T_{MIT} in these films) for 1−3 uc indicates an increase of the magnetic exchange interaction, while the large difference between T_C and T_{MIT} shows that the ferromagnetic layers are magnetically decoupled from the antiferromagnetic layer underneath. Starting from 4 uc thickness, the magnetic moment increases linearly with a slope of 3.8 μ_B/Mn, indicated by the red line in Figure 4c, similar to the $LaMnO_3$ buffer layer case but shifted by 3 uc. We mention here the possibility for frustration at the interface, which was found to be present in $La_{1-x}Sr_xMnO_3/La_{0.6}Sr_{0.4}FeO_3$ multilayers, where $La_{0.6}Sr_{0.4}FeO_3$ is an antiferromagnetic system displaying a C-type canted antiferromagnetic spin state that leads to spin frustration at the $La_{1-x}Sr_xMnO_3$ interface and to more complex spin configurations.[53] In our situation, we expect $La_{0.45}Sr_{0.55}MnO_3$ to be in an A-type antiferromagnetic state, consisting of ferromagnetic spin planes coupled antiferromagnetically along the [001] direction. Such a magnetic spin configuration should not lead to spin frustration at the $La_{0.8}Sr_{0.2}MnO_3$ interface.

To better understand the magnetic and electronic properties of the $La_{0.8}Sr_{0.2}MnO_3$ films, we carried out X-ray magnetic spectroscopy measurements. In Figure 5a,b, we show the evolution of the nonpolarized XAS spectra with thickness for the films grown on the $LaMnO_3$ and $La_{0.45}Sr_{0.55}MnO_3$ buffer layers, respectively. For the case of the films grown on $LaMnO_3$, we find no significant changes in the spectra across the sample series,

which show features characteristic of fully oxidized $La_{0.8}Sr_{0.2}MnO_3$.[54,55] (The spectra corresponding to the 0 and 10 uc samples were collected at the X-Treme beamline and show a different peak amplitude, attributed to different background and measurement conditions between the two endstations; we aligned the energy scale between these two sets of measurements by matching the peak energy of the 10 uc film to that of the 5 uc). Although one may expect a small shift in the peak energy position when going from $LaMnO_3$ to $La_{0.8}Sr_{0.2}MnO_3$, the shift is relatively small,[56] compounded by the fact that the $LaMnO_3$ film is itself slightly doped. The corresponding normalized XMCD spectra are shown in Figure 5c. Similar to XAS, we find no significant changes in the shape and amplitude of the XMCD spectra; the 0 and 10 uc samples show a reduced and an enhanced XMCD signal, respectively. These results confirm that the magnetic moment originates from the Mn cations and are in agreement with the bulk magnetometry results showing full magnetic moment of the $La_{0.8}Sr_{0.2}MnO_3$ film: since the spectra are collected in TEY, which has a sensitivity of around 3−5 nm due to the limited electron mean free path, and is therefore representative of the magnetic state of the surface layers,[57] a constant XMCD signal with thickness confirms that each added layer is magnetic. Interestingly, since the amplitude of the $LaMnO_3$ buffer layer XMCD is comparable to that of the other samples in the series and the XMCD amplitudes are normalized to the XAS spectra, our results suggest that the magnetic moment in $LaMnO_3$ arises from the surface layer. The $La_{0.45}Sr_{0.55}MnO_3$ sample series was measured at the SIM beamline, with the exception of the 5 uc, measured at X-

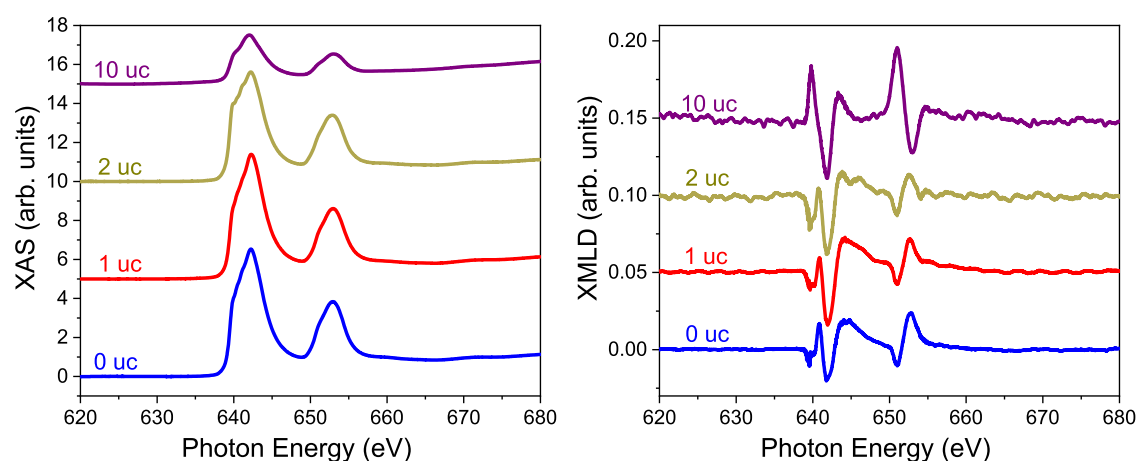**Figure 7.** Average XAS (left) and XMLD (right) scans for samples 0, 1, 2, and 10 uc $La_{0.8}Sr_{0.2}MnO_3/La_{0.45}Sr_{0.55}MnO_3$ taken at 20 K. The XMLD spectra were normalized to the XAS maximum value. Spectra are shifted vertically for clarity of display.

Treme. The shape of the main peak at 642 eV is an indication that the films are stoichiometric and fully oxidized, with Mn present in a mixed 3+/4+ valence state.[56] Figure 5d shows the corresponding XMCD spectra. Consistent with the magnetometry results, the 0, 1, and 2 uc samples show no XMCD signal (the residual signal for 0 uc results from a slight difference in amplitude for the circular right and left light that could not be corrected in the data and does not have the expected XMCD energy variation), while the 5 uc sample displays a strong magnetic dichroic response, but with an amplitude that is lower than the case of the $LaMnO_3$ series. These results support the conclusion that the magnetic signal arises from the top two unit cells and is slightly reduced by the zero XMCD signal contribution from the antiferromagnetic $La_{0.8}Sr_{0.2}MnO_3/La_{0.45}Sr_{0.55}MnO_3$ films underneath.

Magnetic exchange in these materials is generally understood in terms of orbital occupancy, according to the Goodenough–Kanamori rules.[12,58] In particular, doping and strain play fundamental roles in determining which of the spin exchange mechanisms, double exchange or superexchange, dominates the magnetic interaction since the orbital structure depends strongly on those parameters. In order to probe the orbital character of the $La_{0.8}Sr_{0.2}MnO_3/La_{0.45}Sr_{0.55}MnO_3$ heterostructures, we carried out X-ray absorption measurements with linearly polarized light, which probes the available density of states along the electric field direction.[59] The XAS spectra measured at 300 K, above the Curie temperature to avoid the magnetic contribution, are shown in Figure 6a,d for the O K-edge and Mn L-edge, respectively.

The O K-edge shows the general shape typical for $La_{0.8}Sr_{0.2}MnO_3$, with pre-edge peaks (A, B) associated with O 2p orbitals hybridized with Mn 3d and higher energy peaks, C, D, associated with O 2p orbitals hybridized with La and Sr orbitals, respectively.[56] Of interest here are the pre-edge peaks, in the range 527−533 eV, which are argued to reflect more directly the unoccupied density of states of the Mn 3d states, since the excitation occurs at the oxygen site.[60] Two different assignments of these peaks to the Mn orbitals states have been presented in the literature, in one case where peak A is assigned to the partially filled $e_g^\uparrow$ band and peak B to transitions into empty $t_{2g}^\downarrow$ and $e_g^\downarrow$ states;[56,61,62] another assignment ascribes peak A to the partially filled $e_g^\uparrow$ band and empty $t_{2g}^\downarrow$ and peak B to transitions into $e_g^\downarrow$ states.[63] Our results are not able to address this

controversy; however, we can extract the following conclusions from our data.

(i) One finds a shift to higher energies of the O pre-edge features associated with the $e_g^\uparrow$ band when going from 0, 1, and 2 uc $La_{0.45}Sr_{0.55}MnO_3$ to 5 and 10 uc $La_{0.8}Sr_{0.2}MnO_3$ (Figure 6b); this is expected based on band filling, since with decreasing hole doping the electron occupation of the $e_g^\uparrow$ band increases, resulting in a decrease in the unoccupied density of states.

(ii) One finds that the leading edge of the X-ray absorption spectra occurs at lower energies for the in-plane polarized light, while the difference is significantly reduced for the 5 and 10 uc films; this can be more easily seen as a shift to higher energies of the spectral weight of the linear dichroic signal at the $e_g^\uparrow$ band, Figure 6c. This behavior indicates a reduction in the asymmetry of the occupancy of in-plane and out-of-plane orbitals at larger $La_{0.8}Sr_{0.2}MnO_3$ thicknesses, consistent with what is expected for the ferromagnetic state.[64] Furthermore, the role of strain is that of shifting the relative energy position of the two $e_g^\uparrow$ orbitals, z^2 and $x^2 - y^2$, with compressive (negative) strain favoring the $x^2 - y^2$ orbitals.[65] We note that, given that both layers have the same in-plane lattice parameter and given that the lattice parameter of $La_{1-x}Sr_xMnO_3$ changes with Sr doping, the $La_{0.45}Sr_{0.55}MnO_3$ buffer layer and the $La_{0.8}Sr_{0.2}MnO_3$ top layer are subjected to different in-plane strains. Taking the pseudocubic lattice parameters for $La_{0.45}Sr_{0.55}MnO_3$ and $La_{0.8}Sr_{0.2}MnO_3$ as 3.84 and 3.89 Å, respectively,[13,34,39] one obtains in-plane strains of −1.69 and −0.39%, respectively. Thus, our results agree with the expectations and are consistent with the magnetic behavior, i.e., an antiferromagnetic in-plane metallic A-type state for $La_{0.45}Sr_{0.55}MnO_3$ and a ferromagnetic isotropic state for $La_{0.8}Sr_{0.2}MnO_3$.

(iii) In terms of the thickness evolution, one finds that up to 2 uc $La_{0.8}Sr_{0.2}MnO_3$ the XLD spectra in Figure 6e remain essentially unchanged (although in these cases, a significant signal contribution from the underlying $La_{0.45}Sr_{0.55}MnO_3$ layer should be present), while for 5 uc, which is expected to have a strongly reduced $La_{0.45}Sr_{0.55}MnO_3$ signal contribution due to the limited electron escape depth, a strong modification in the XAS spectra is observed, starting to resemble the 10 uc $La_{0.8}Sr_{0.2}MnO_3$ spectra.

(iv) The integral of the linear dichroism over the Mn $L_{2,3}$ edge, Figure 6e, gives the preferred hole orbital occupation according to the linear dichroism sum rule $D_L = \int_{L_2+L_3}(\mu_{ab} - \mu_c)\,dE / \int_{L_2+L_3}(2\mu_{ab} + \mu_c)dE \propto \sum \langle l_z^2 - 2\rangle_i$, where μ_{ab} and μ_c are the X-ray absorption along the in-plane and out-of-plane directions, respectively, l_z is the quantum orbital number, with $l_z = 0$ for the $3d_{3z^2-r^2}$ orbital and $l_z = 2$ for $3d_{x^2-y^2}$.[66] A positive value for D_L indicates a preferential hole occupation of the $x^2 - y^2$ orbitals. Based on this sum rule, one finds, qualitatively, that for 0−2 uc $La_{0.8}Sr_{0.2}MnO_3$ the in-plane $x^2 - y^2$ orbitals are preferentially occupied by hole carriers,[61,67] while for 5 and 10 uc, there is a change in the orbital character to a predominant hole occupation of the out-of-plane orbitals. The changes in the orbital character are in general qualitative agreement with the O pre-edge spectral features.

We also carried out magnetic linear dichroism (XMLD) measurements for 0, 1, 2, and 10 uc $La_{0.8}Sr_{0.2}MnO_3$/$La_{0.45}Sr_{0.55}MnO_3$ at 20 K, as shown in Figure 7. The XMLD signal is normalized to the XAS peak intensity, and these measurements are taken with a large beam spot (of about 1 mm in lateral size), averaging over a large area of the sample, i.e., it is an average over the antiferromagnetic multidomain state of the sample. Assuming that for all samples there is a similar antiferromagnetic domain distribution, these data tell us that the amplitude of the XMLD signal remains approximately constant with increasing film thickness, which indicates that each added layer contributes similarly to the XMLD signal (otherwise, the relative magnetic contribution to the total signal would drop). These data further support our conclusion that the top $La_{0.8}Sr_{0.2}MnO_3$ layer is in an antiferromagnetic state at lower thicknesses, as discussed above.

From these observations, in combination with the magnetic behavior, we conclude that $La_{0.8}Sr_{0.2}MnO_3$ films up to 3 uc thickness have a similar electronic and magnetic structure as the $La_{0.45}Sr_{0.55}MnO_3$ buffer layer, characterized by a preferential hole occupation of the $x^2 - y^2$ orbitals, large in-plane conductivity, and an A-type antiferromagnetic ordering. At larger thicknesses, a transition to a preferential occupation of out-of-plane orbitals occurs, where a spectrum similar to that reported for the fully polarized ferromagnetic state is observed,[68] even if an equal population of both in-plane and out-of-plane orbitals were expected.[69]

The two different buffer layers, therefore, lead to two distinct magnetic behaviors for the top $La_{0.8}Sr_{0.2}MnO_3$ films. In the case of LaMnO$_3$, the $La_{0.8}Sr_{0.2}MnO_3$ films are fully magnetically polarized starting from 1 uc, with a magnetic critical temperature that is much higher than that of the single buffer layer, indicating the presence of a strong magnetic coupling dominated by the top $La_{0.8}Sr_{0.2}MnO_3$. Since the LaMnO$_3$ film is insulating, we attribute the magnetic coupling to be dominated by double exchange at the interface between the two systems. In the case of the $La_{0.45}Sr_{0.55}MnO_3$ buffer layer, we find that the $La_{0.8}Sr_{0.2}MnO_3$ film adopts the metallic antiferromagnetic state of the buffer layer up to a thickness of 3−4 uc and a sudden transition to a ferromagnetic state above this thickness, manifested in the linear dichroic data by a sudden modification of the electronic structure from 2 to 5 uc films. We explain the interfacial antiferromagnetic metallic state as driven by extended delocalized charge transfer between $La_{0.45}Sr_{0.55}MnO_3$ and $La_{0.8}Sr_{0.2}MnO_3$, which operates up to three unit cells beyond

the interface. At larger thicknesses, the $La_{0.8}Sr_{0.2}MnO_3$ adopts its ferromagnetic ground state with a full bulk moment and critical temperature independent of the underlying manganite film. In both instances, the $La_{0.8}Sr_{0.2}MnO_3$ films are fully magnetically polarized, starting from the single unit cell. One possible common mechanism driving the magnetic behavior of the top $La_{0.8}Sr_{0.2}MnO_3$ films toward bulk behavior may be the onset of oxygen octahedral rotations promoted by the LaMnO$_3$ buffer layer and the first 3−4 unit cells $La_{0.8}Sr_{0.2}MnO_3$/$La_{0.45}Sr_{0.55}MnO_3$, which agrees with the length scale for bond angle relaxation of the oxygen octahedral tilt of 4 unit cells found for LaMnO$_3$/SrTiO$_3$ superlattices.[70]

Our results are highly relevant for device applications since they provide an approach to using the same material platform to create $La_{0.8}Sr_{0.2}MnO_3$ films that are fully magnetically polarized down to 1 uc either on conducting buffer layers ($La_{0.45}Sr_{0.55}MnO_3$) or on magnetic but insulating layers (LaMnO$_3$). We anticipate as well that the results found here may be applicable to the wider doping range where $La_{1-x}Sr_xMnO_3$ is in a ferromagnetic state, including optimally doped $La_{1-x}Sr_xMnO_3$, and to the wider manganite perovskite family.

4. CONCLUSIONS

In conclusion, we have studied the evolution of the magnetic moment of ultrathin $La_{0.8}Sr_{0.2}MnO_3$ films grown on insulating LaMnO$_3$ and conducting $La_{0.45}Sr_{0.55}MnO_3$ buffer layers. Although both systems are nominally antiferromagnetic, we find a significant magnetic moment in the LaMnO$_3$ buffer layer, a result similar to that reported previously in the literature. For $La_{0.8}Sr_{0.2}MnO_3$/LaMnO$_3$, a metallic state and bulk-like magnetic moment are observed for $La_{0.8}Sr_{0.2}MnO_3$ thicknesses down to 1 uc. The two layers are magnetically coupled, but the magnetic properties are dominated by the top $La_{0.8}Sr_{0.2}MnO_3$ film, including bulk-like magnetic moments and high critical temperatures that do not correspond to those of the bare LaMnO$_3$ film. For the case of $La_{0.8}Sr_{0.2}MnO_3$/$La_{0.45}Sr_{0.55}MnO_3$, we observe an antiferromagnetic ground state up to 3 uc, above which a ferromagnetic ground state for the subsequent $La_{0.8}Sr_{0.2}MnO_3$ layers emerges. The X-ray absorption spectroscopy results show a sudden change in the electronic structure from 2 to 5 uc, consistent with the observed change in the magnetic properties. Our results show that the properties of ultrathin $La_{0.8}Sr_{0.2}MnO_3$ films can be tailored by a suitable choice of buffer layers to yield bulk-like magnetic polarization and high critical temperatures, down to the unit cell thickness range, paving the way to fully exploring the unique electronic properties of this class of strongly correlated oxide materials.

■ ASSOCIATED CONTENT

Data Availability Statement

The data underlying this study are openly available at the PSI Public Data Repository database at doi.psi.ch/detail/10.16907/b927e658-d5b2-4892-aebf-6d831956939d.

■ AUTHOR INFORMATION

Corresponding Author

Carlos A. F. Vaz − *Swiss Light Source, Paul Scherrer Institut, Villigen 5232, Switzerland;* orcid.org/0000-0002-6209-8918; Email: carlos.vaz@psi.ch

Authors

Federico Stramaglia − *Swiss Light Source, Paul Scherrer Institut, Villigen 5232, Switzerland;* ⊙ orcid.org/0000-0001-6204-7064

Gyanendra Panchal − *Swiss Light Source, Paul Scherrer Institut, Villigen 5232, Switzerland;* ⊙ orcid.org/0000-0001-5208-8831

Frithjof Nolting − *Swiss Light Source, Paul Scherrer Institut, Villigen 5232, Switzerland*

Complete contact information is available at:
https://pubs.acs.org/10.1021/acsami.3c14031

Notes

The authors declare no competing financial interest.

◼ REFERENCES

(1) Vaz, C. A. F.; Walker, F. J.; Ahn, C. H.; Ismail-Beigi, S. Intrinsic Interfacial Phenomena in Manganite Heterostructures. *J. Phys.: Condens. Matter* **2015**, *27*, No. 123001.

(2) Zubko, P.; Gariglio, S.; Gabay, M.; Ghosez, P.; Triscone, J.-M. Interface Physics in Complex Oxide Heterostructures. *Annu. Rev. Condens. Matter Phys.* **2011**, *2*, 141.

(3) Vaz, C. A. F.; Bland, J. A. C.; Lauhoff, G. Magnetism in Ultrathin Film Structures. *Rep. Prog. Phys.* **2008**, *71*, No. 056501.

(4) Vaz, C. A. F.; Shin, Y. J.; Bibes, M.; Rabe, K. M.; Walker, F. J.; Ahn, C. H. Epitaxial Ferroelectric Interfacial Devices. *Appl. Phys. Rev.* **2021**, *8*, No. 041308.

(5) Burton, J. D.; Tsymbal, E. Y. Prediction of Electrically Induced Magnetic Reconstruction at the Manganite/Ferroelectric Interface. *Phys. Rev. B* **2009**, *80*, No. 174406.

(6) Vaz, C. A. F.; Hoffman, J.; Ahn, C. H.; Ramesh, R. Magnetoelectric Coupling Effects in Multiferroic Complex Oxide Composite Structures. *Adv. Mater.* **2010**, *22*, 2900−2918.

(7) Zhou, J.; Tra, V. T.; Dong, S.; Trappen, R.; Marcus, M. A.; Jenkins, C.; Frye, C.; Wolfe, E.; White, R.; Polisetty, S.; Lin, J.-Y.; LeBeau, J. M.; Chu, Y.-H.; Holcomb, M. B. Thickness Dependence of La$_{0.7}$Sr$_{0.3}$MnO$_3$/Pb(Zr$_{0.2}$Ti$_{0.8}$)O$_3$ Magnetoelectric Interfaces. *Appl. Phys. Lett.* **2015**, *107*, No. 141603.

(8) Meyer, T. L.; Herklotz, A.; Lauter, V.; Freeland, J. W.; Nichols, J.; Guo, E.-J.; Lee, S.; Ward, T. Z.; Balke, N.; Kalinin, S. V.; Fitzsimmons, M. R.; Lee, H. N. Enhancing Interfacial Magnetization with a Ferroelectric. *Phys. Rev. B* **2016**, *94*, No. 174432.

(9) Paudel, B.; Vasiliev, I.; Hammouri, M.; Karpov, D.; Chen, A.; Lauter, V.; Fohtung, E. Strain Vs. Charge Mediated Magnetoelectric Coupling Across the Magnetic Oxide/Ferroelectric Interfaces. *RSC Adv.* **2019**, *9*, 13033−13041.

(10) Qin, P.-X.; Yan, H.; Wang, X.-N.; Feng, Z.-X.; Guo, H.-X.; Zhou, X.-R.; Wu, H.-J.; Zhang, X.; Leng, Z.-G.-G.; Chen, H.-Y.; Liu, Z.-Q. Noncollinear Spintronics and Electric-Field Control: a Review. *Rare Met.* **2020**, *39*, 95−112.

(11) Vaz, C. A. F.; Hoffman, J.; Segal, Y.; Reiner, J. W.; Grober, R. D.; Zhang, Z.; Ahn, C. H.; Walker, F. J. Origin of the Magnetoelectric Coupling Effect in Pb(Zr$_{0.2}$Ti$_{0.8}$)O$_3$/La$_{0.8}$Sr$_{0.2}$MnO$_3$ Multiferroic Heterostructures. *Phys. Rev. Lett.* **2010**, *104*, No. 127202.

(12) Goodenough, J. B. Theory of the Role of Covalence in the Perovskite-Type Manganites [La, M(II)]MnO$_3$. *Phys. Rev.* **1955**, *100*, 564−573.

(13) Urushibara, A.; Moritomo, Y.; Arima, T.; Asamitsu, A.; Kido, G.; Tokura, Y. Insulator-Metal Transition and Giant Magnetoresistance in La$_{1−x}$Sr$_x$MnO$_3$. *Phys. Rev. B* **1995**, *51*, 14103−14109.

(14) Imada, M.; Fujimori, A.; Tokura, Y. Metal-Insulator Transitions. *Rev. Mod. Phys.* **1998**, *70*, 1039.

(15) Yu, X.; Jin, S.; Li, H.; Guan, X.; Gu, X.; Liu, X. High Room-Temperature TCR and MR of La$_{1−x}$Sr$_x$MnO$_3$ Thin Films for Advanced Uncooled Infrared Bolometers and Magnetic Sensors. *Appl. Surf. Sci.* **2021**, *570*, No. 151221.

(16) Dadhich, H.; Rajyaguru, B.; Gadani, K.; Goswami, H.; Rathod, V. R.; Shrimali, V. G.; Mukherjee, S.; Asokan, K.; Shah, N. A.; Solanki, P. S. Thermionic Emission Assisted Charge Conduction Mechanisms Across LaMnO$_3$/La$_{0.7}$Ca$_{0.3}$MnO$_3$ Interface of Manganite Thin Film Structure. *Curr. Appl. Phys.* **2023**, *50*, 1−12.

(17) Feng, Y.; Jin, K.-j.; Gu, L.; He, X.; Ge, C.; Zhang, Q.-h.; He, M.; Guo, Q.-l.; Wan, Q.; He, M.; Lu, H.-b.; Yang, G. Insulating Phase at Low Temperature in Ultrathin La$_{0.8}$Sr$_{0.2}$MnO$_3$ Films. *Sci. Rep.* **2016**, *6*, No. 22382.

(18) Chen, H.; Yu, Y.; Wang, Z.; et al. Thickness-Driven First-Order Phase Transitions in Manganite Ultrathin Films. *Phys. Rev. B* **2019**, *99*, No. 214419.

(19) Izumi, M.; Ogimoto, Y.; Okimoto, Y.; Manako, T.; Ahmet, P.; Nakajima, K.; Chikyow, T.; Kawasaki, M.; Tokura, Y. Insulator-Metal Transition Induced by Interlayer Coupling in La$_{0.6}$Sr$_{0.4}$MnO$_3$/SrTiO$_3$ Superlattices. *Phys. Rev. B* **2001**, *64*, No. 064429.

(20) Yamada, H.; Ogawa, Y.; Ishii, Y.; Sato, H.; Kawasaki, M.; Akoh, H.; Tokura, Y. Engineered Interface of Magnetic Oxides. *Science* **2004**, *305*, 646−648.

(21) Mundy, J. A.; Hikita, Y.; Hidaka, T.; Yajima, T.; Higuchi, T.; Hwang, H. Y.; Muller, D. A.; Kourkoutis, L. F. Visualizing the Interfacial Evolution from Charge Compensation to Metallic Screening across the Manganite Metal−Insulator Transition. *Nat. Commun.* **2014**, *5*, No. 3464. DOI: 10.1038/ncomms4464.

(22) Peng, R.; Xu, H. C.; Xia, M.; Zhao, J. F.; Xie, X.; Xu, D. F.; Xie, B. P.; Feng, D. L. Tuning the Dead-Layer Behavior of La$_{0.67}$Sr$_{0.33}$MnO$_3$/SrTiO$_3$ via Interfacial Engineering. *Appl. Phys. Lett.* **2014**, *104*, No. 081606.

(23) Monsen, Å.; Boschker, J. E.; Macià, F.; Wells, J. W.; Nordblad, P.; Kent, A. D.; Mathieu, R.; Tybell, T.; Wahlström, E. Thickness Dependence of Dynamic and Static Magnetic Properties of Pulsed Laser Deposited La$_{0.7}$Sr$_{0.3}$MnO$_3$ Films on SrTiO$_3$(001). *J. Magn. Magn. Mater.* **2014**, *369*, 197−204.

(24) Bruno, F. Y.; Garcia-Barriocanal, J.; Varela, M.; Nemes, N. M.; Thakur, P.; Cezar, J. C.; Brookes, N. B.; Rivera-Calzada, A.; Garcia-Hernandez, M.; Leon, C.; Okamoto, S.; Pennycook, S. J.; Santamaria, J. Electronic and Magnetic Reconstructions in La$_{1−x}$Sr$_x$MnO$_3$/SrTiO$_3$ Heterostructures: A Case of Enhanced Interlayer Coupling Controlled by the Interface. *Phys. Rev. Lett.* **2011**, *106*, No. 147205.

(25) Lee, J.-S.; Arena, D. A.; Yu, P.; Nelson, C. S.; Fan, R.; Kinane, C. J.; Langridge, S.; Rossell, M. D.; Ramesh, R.; Kao, C.-C. Hidden Magnetic Configuration in Epitaxial La$_{1−x}$Sr$_x$O$_3$ Films. *Phys. Rev. Lett.* **2010**, *105*, No. 257204.

(26) Tebano, A.; Orsini, A.; Medaglia, P. G.; Di Castro, D.; Balestrino, G.; Freelon, B.; Bostwick, A.; Chang, Y. J.; Gaines, G.; Rotenberg, E.; Saini, N. L. Preferential Occupation of Interface Bands in La$_{2/3}$Sr$_{1/3}$MnO$_3$ Films as Seen via Angle-Resolved Photoemission. *Phys. Rev. B* **2010**, *82*, No. 214407.

(27) Tebano, A.; Aruta, C.; Sanna, S.; Medaglia, P. G.; Balestrino, G.; Sidorenko, A. A.; De Renzi, R.; Ghiringhelli, G.; Braicovich, L.; Bisogni, V.; Brookes, N. B. Evidence of Orbital Reconstruction at Interfaces in

Ultrathin La$_{0.67}$Sr$_{0.33}$MnO$_3$ Films. *Phys. Rev. Lett.* **2008**, *100*, No. 137401.

(28) Boschker, H.; Verbeeck, J.; Egoavil, R.; Bals, S.; van Tendeloo, G.; Huijben, M.; Houwman, E. P.; Koster, G.; Blank, D. H. A.; Rijnders, G. Preventing the Reconstruction of the Polar Discontinuity at Oxide Heterointerfaces. *Adv. Funct. Mater.* **2012**, *22*, 2235−2240.

(29) Huijben, M.; Martin, L. W.; Chu, Y.-H.; Holcomb, M. B.; Yu, P.; Rijnders, G.; Blank, D. H. A.; Ramesh, R. Critical Thickness and Orbital Ordering in Ultrathin La$_{0.7}$Sr$_{0.3}$MnO$_3$ Films. *Phys. Rev. B* **2008**, *78*, No. 094413.

(30) Gao, W. W.; Hu, F. X.; Shen, B. G.; Sun, J. R. Modulation of the Magnetic/Conductive Dead Layer at the Manganites-SrTiO$_3$ Interface. *J. Appl. Phys.* **2015**, *117*, No. 17C733.

(31) Piamonteze, C.; Bern, F.; Avula, S. R. V.; Studniarek, M.; Autieri, C.; Ziese, M.; Lindfors-Vrejoiu, I. Ferromagnetic Order of Ultra-thin La$_{0.7}$Ba$_{0.3}$MnO$_3$ Sandwiched Between SrRuO$_3$ Layers. *Appl. Phys. Lett.* **2021**, *118*, No. 152408.

(32) Chen, B.; Xu, H.; Ma, C.; Mattauch, S.; Lan, D.; Jin, F.; Guo, Z.; Wan, S.; Chen, P.; Gao, G.; Chen, F.; Su, Y.; Wu, W. All-Oxide-Based Synthetic Antiferromagnets Exhibiting Layer-Resolved Magnetization Reversal. *Science* **2017**, *357*, 191−194.

(33) Vaz, C. A. F.; Hoffman, J.; Segal, Y.; Marshall, M. S. J.; Reiner, J. W.; Zhang, Z.; Grober, R. D.; Walker, F. J.; Ahn, C. H. Control of Magnetism in Pb(Zr$_{0.2}$Ti$_{0.8}$)O$_3$/La$_{0.8}$Sr$_{0.2}$MnO$_3$ Multiferroic Heterostructures (invited). *J. Appl. Phys.* **2011**, *109*, No. 07D905.

(34) Vaz, C. A. F.; Moyer, J. A.; Arena, D. A.; Ahn, C. H.; Henrich, V. E. Magnetic and Electronic Structure of Ultrathin La$_{1-x}$Sr$_x$MnO$_3$ Films at Half Doping. *Phys. Rev. B* **2014**, *90*, No. 024414.

(35) Kareev, M.; Prosandeev, S.; Liu, J.; Gan, C.; Kareev, A.; Freeland, J. W.; Xiao, M.; Chakhalian, J. Atomic Control and Characterization of Surface Defect States of TiO2 Terminated SrTiO$_3$ Single Crystals. *Appl. Phys. Lett.* **2008**, *93*, No. 061909.

(36) Zhang, J.; Doutt, D.; Merz, T.; Chakhalian, J.; Kareev, M.; Liu, J.; Brillson, L. J. Depth-Resolved Subsurface Defects in Chemically Etched SrTiO$_3$. *Appl. Phys. Lett.* **2009**, *94*, No. 092904.

(37) van der Pauw, L. J. A Method of Measuring Specific Resistivity and Hall Effect of Discs of Arbitrary Shape. *Philips Res. Repts.* **1958**, *13*, 1−9.

(38) van der Pauw, L. J. A Method of Measuring the Resistivity and Hall Coefficient of Lamellae of Arbitrary Shape. *Philips Technol. Rev.* **1958**, *20*, 220−224.

(39) Chmaissem, O.; Dabrowski, B.; Kolesnik, S.; Mais, J.; Jorgensen, J. D.; Short, S. Structural and Magnetic Phase Diagrams of La$_{1-x}$Sr$_x$MnO$_3$ and Pr$_{1-y}$Sr$_y$MnO$_3$. *Phys. Rev. B* **2003**, *67*, No. 094431.

(40) Wang, X. R.; Li, C. J.; Lü, W. M.; Paudel, T. R.; Leusink, D. P.; Hoek, M.; Poccia, N.; Vailionis, A.; Venkatesan, T.; Coey, J. M. D.; Tsymbal, E. Y.; Hilgenkamp, H. Imaging and Control of Ferromagnetism in LaMnO$_3$/SrTiO$_3$ Heterostructures. *Science* **2015**, *349*, 716−719.

(41) Wu, L.; Li, C.; Chen, M.; et al. Interface-Induced Enhancement of Ferromagnetism in Insulating LaMnO$_3$ Ultrathin Films. *ACS Appl. Mater. Interfaces* **2017**, *9*, 44931−44937. PMID: 29236463

(42) Roqueta, J.; Pomar, A.; Balcells, L.; Frontera, C.; Valencia, S.; Abrudan, R.; Bozzo, B.; Konstantinović, Z.; Santiso, J.; Martínez, B. Strain-Engineered Ferromagnetism in LaMnO$_3$ Thin Films. *Cryst. Growth Des.* **2015**, *15*, 5332−5337.

(43) Banerjee, H.; Aichhorn, M. Emergence of a Ferromagnetic Insulating State in LaMnO$_3$/SrTiO$_3$ Heterostructures: Role of Strong Electronic Correlations and Strain. *Phys. Rev. B* **2020**, *101*, No. 241112.

(44) Marton, Z.; A Seo, S. S.; Egami, T.; Lee, H. N. Growth Control of Stoichiometry in LaMnO$_3$ Epitaxial Thin Films by Pulsed Laser Deposition. *J. Cryst. Growth* **2010**, *312*, 2923−2927.

(45) Kim, H. S.; Christen, H. M. Controlling the Magnetic Properties of LaMnO$_3$ Thin Films on SrTiO$_3$(100) by Deposition in a O$_2$/Ar Gas Mixture. *J. Phys.: Condens. Matter* **2010**, *22*, No. 146007.

(46) Zhao, R.; Jin, K.; Xu, Z.; Guo, H.; Wang, L.; Ge, C.; Lu, H.; Yang, G. The Oxygen Vacancy Effect on the Magnetic Property of the LaMnO$_{3-\delta}$ Thin Films. *Appl. Phys. Lett.* **2013**, *102*, No. 122402.

(47) Niu, W.; Liu, W.; Gu, M.; et al. Direct Demonstration of the Emergent Magnetism Resulting from the Multivalence Mn in a LaMnO$_3$ Epitaxial Thin Film System. *Adv. Electron. Mater.* **2018**, *4*, No. 1800055.

(48) Stramaglia, F.; Panchal, G.; Nolting, F.; Vaz, C. A. F. Role of Interdiffusion on the Magnetism of Ultrathin LaMnO$_3$ Films. **2024**, in press.

(49) Lofland, S. E.; Bhagat, S. M.; Ghosh, K.; Greene, R. L.; Karabashev, S. G.; Shulyatev, D. A.; Arsenov, A. A.; Mukovskii, Y. Magnetic Transition and Electronic Transport in Colossal Magnetoresistance Perovskites. *Phys. Rev. B* **1997**, *56*, 13705−13707.

(50) Santos, T. S.; May, S. J.; Robertson, J. L.; Bhattacharya, A. Tuning Between the Metallic Antiferromagnetic and Ferromagnetic Phases of La$_{1-x}$Sr$_x$MnO$_3$ Near x = 0.5 by Digital Synthesis. *Phys. Rev. B* **2009**, *80*, 155114.

(51) Segal, Y.; Garrity, K. F.; Vaz, C. A. F.; Hoffman, J. D.; Walker, F. J.; Ismail-Beigi, S.; Ahn, C. H. Dynamic Evanescent Phonon Coupling Across the La$_{1-x}$Sr$_x$MnO$_3$/SrTiO$_3$ Interface. *Phys. Rev. Lett.* **2011**, *107*, No. 105501.

(52) Panchal, G.; Stramaglia, F.; Nolting, F.; Vaz, C. A. F. Charge-exchange-driven Interfacial Antiferromagnetic Ground State in La$_{0.8}$Sr$_{0.2}$MnO$_3$ Ultrathin Films. **2023**, Unpublished.

(53) Izumi, M.; Ogimoto, Y.; Konishi, Y.; Manako, T.; Kawasaki, M.; Tokura, Y. Perovskite Superlattices as Tailored Materials of Correlated Electrons. *Mater. Sci. Eng. B* **2001**, *84*, 53.

(54) Gilbert, B.; Frazer, B. H.; Belz, A.; Conrad, P. G.; Nealson, K. H.; Haskel, D.; Lang, J. C.; Srajer, G.; De Stasio, G. Multiple Scattering Calculations of Bonding and X-ray Absorption Spectroscopy of Manganese Oxides. *J. Phys. Chem. A* **2003**, *107*, 2839−2847.

(55) Burnus, T.; Hu, Z.; Hsieh, H. H.; Joly, V. L. J.; Joy, P. A.; Haverkort, M. W.; Wu, H.; Tanaka, A.; Lin, H.-J.; Chen, C. T.; Tjeng, L. H. Local Electronic Structure and Magnetic Properties of LaMn$_{0.5}$Co$_{0.5}$O$_3$ Studied by X-ray Absorption and Magnetic Circular Dichroism Spectroscopy. *Phys. Rev. B* **2008**, *77*, No. 125124.

(56) Abbate, M.; de Groot, F. M. F.; Fuggle, J. C.; Fujimori, A.; Strebel, O.; Lopez, F.; Domke, M.; Kaindl, G.; Sawatzky, G. A.; Takano, M.; Takeda, Y.; Eisaki, H.; Uchida, S. Controlled-Valence Properties of La$_{1-x}$Sr$_x$FeO$_3$ and La$_{1-x}$Sr$_x$MnO$_3$ Studied by Soft-X-ray Absorption Spectroscopy. *Phys. Rev. B* **1992**, *46*, 4511−4519.

(57) Seah, M. P.; Dench, W. A. Quantitative Electron Spectroscopy of Surfaces: A Standard Data Base for Electron Inelastic Mean Free Paths in Solids. *Surf. Interface Anal.* **1979**, *1*, 2−11.

(58) Kanamori, J. Superexchange Interaction and Symmetry Properties of Electron Orbitals. *J. Phys. Chem. Solids* **1959**, *10*, 87−98.

(59) Stöhr, J.; Siegmann, H. C. *Magnetism*; Springer-Verlag: Berlin, 2006.

(60) de Groot, F. M. F.; Grioni, M.; Fuggle, J. C.; Ghijsen, J.; Sawatzky, G. A.; Petersen, H. Oxygen 1s X-ray-Absorption Edges of Transition-Metal Oxides. *Phys. Rev. B* **1989**, *40*, 5715−5723.

(61) Aruta, C.; Ghiringhelli, G.; Tebano, A.; Boggio, N. G.; Brookes, N. B.; Medaglia, P. G.; Balestrino, G. Strain Induced X-ray Absorption Linear Dichroism in La$_{0.7}$Sr$_{0.3}$MnO$_3$ Thin Films. *Phys. Rev. B* **2006**, *73*, No. 235121.

(62) Saitoh, T.; Bocquet, A. E.; Mizokawa, T.; Namatame, H.; Fujimori, A.; Abbate, M.; Takeda, Y.; Takano, M. Electronic Structure of La$_{1-x}$Sr$_x$MnO$_3$ Studied by Photoemission and X-ray-Absorption Spectroscopy. *Phys. Rev. B* **1995**, *51*, 13942−13951.

(63) Pellegrin, E.; Tjeng, L. H.; de Groot, F. M. F.; Hesper, R.; Sawatzky, G. A.; Moritomo, Y.; Tokura, Y. Soft X-Ray Magnetic Circular Dichroism Study of the Colossal Magnetoresistance Compound La$_{1-x}$Sr$_x$MnO−3. *J. Electron Spectrosc. Relat. Phenom.* **1997**, *86*, 115.

(64) Konishi, Y.; Fang, Z.; Izumi, M.; Manako, T.; Kasai, M.; Kuwahara, H.; Kawasaki, M.; Terakura, K.; Tokura, Y. Orbital-State-Mediated Phase-Control of Manganites. *J. Phys. Soc. Jpn.* **1999**, *68*, 3790.

(65) Fang, Z.; Solovyev, I. V.; Terakura, K. Phase Diagram of Tetragonal Manganites. *Phys. Rev. Lett.* **2000**, *84*, 3169.

(66) Núñez Regueiro, M. D.; Altarelli, M.; Chen, C. T. X-ray-Absorption Sum Rule for Linear Dichroism: Application to High-T_c Cuprate Oxides. *Phys. Rev. B* **1995**, *51*, 629−631.

(67) Pesquera, D.; Herranz, G.; Barla, A. e. a.; et al. Surface Symmetry-Breaking and Strain Effects on Orbital Occupancy in Transition Metal Perovskite Epitaxial Films. *Nat. Commun.* **2012**, *3*, No. 1189, DOI: 10.1038/ncomms2189.

(68) Aruta, C.; Balestrino, G.; Tebano, A.; Ghiringhelli, G.; Brookes, N. B. Cooperative Enhancement of In-Plane Orbital Ordering by Oxygen Deficiency and In-Plane Tensile Strain in $La_{0.7}Sr_{0.3}MnO_{3-\delta}$ Thin Films. *Europhys. Lett.* **2007**, *80*, No. 37003.

(69) Nanda, B. R. K.; Satpathy, S. Effects of Strain on Orbital Ordering and Magnetism at Perovskite Oxide Interfaces: $LaMnO_3/SrMnO_3$. *Phys. Rev. B* **2008**, *78*, No. 054427.

(70) Zhai, X.; Cheng; Liu, Y.; Schlepütz, C. M.; Dong, S.; Li, H.; Zhang, X.; Chu, S.; Zheng, L.; Zhang, J.; Zhao, A.; Hong, H.; Bhattacharya, A.; Eckstein, J. N.; Zeng, C. Correlating Interfacial Octahedral Rotations with Magnetism in $(LaMnO_3)_N/(SrTiO_3)_N$ Superlattices. *Nat. Commun.* **2014**, *5*, No. 4283.